



# Carbon nanofiber supported Mo<sub>2</sub>C catalysts for hydrodeoxygenation of guaiacol: The importance of the carburization process

E. Ochoa<sup>a</sup>, D. Torres<sup>a</sup>, R. Moreira<sup>b</sup>, J.L. Pinilla<sup>a,\*</sup>, I. Suelves<sup>a</sup>

<sup>a</sup> Instituto de Carboquímica, CSIC, C/ Miguel Luesma Castán 4, Zaragoza 50018, Spain

<sup>b</sup> CIEPQPF, Department of Chemical Engineering, Faculty of Sciences and Technology, University of Coimbra, Rua Sílvio Lima, 3030-790 Coimbra, Portugal

## ARTICLE INFO

### Keywords:

Hydrodeoxygenation  
Molybdenum carbide catalyst  
Carbon nanofibers supported catalysts  
Bio-oils

## ABSTRACT

Molybdenum carbide catalysts supported on carbon nanofibers ( $\beta$ -Mo<sub>2</sub>C/CNF) were synthesized employing different carburization parameters: five temperatures (550–750 °C) and four heating rates (1–10 °C/min) were tested. The carburization process of the Mo precursor in the catalysts was studied by thermogravimetric analysis, X-ray diffraction, X-ray photoelectron spectroscopy, N<sub>2</sub> physisorption, inductively coupled plasma optical emission spectrometry and transmission electron microscopy. The formation of the carbide phase was confirmed by the presence of the oxycarbide and carbide phases which were observed on the surface of all catalysts. Higher carburization temperatures resulted in an increase of the carbide phase content and crystal size at the expenses of the oxycarbide phase disappearance. High carburization temperatures and low heating rates were needed in order to obtain well-defined  $\beta$ -Mo<sub>2</sub>C crystals over the catalysts, which involved a substantial improvement of their catalytic activity in the hydrodeoxygenation of guaiacol.

## 1. Introduction

The development of second-generation bio-fuels continues to be one of the main research topics for mitigating the depletion of fossil fuels and the dramatic increasing of CO<sub>2</sub> in the atmosphere. In particular, lignocellulosic bio-oils cannot be fractional distilled for separation of petrochemical cuts in the current oil industry infrastructure, because they repolymerize upon heating due to the chemical and thermal instability of related with their high oxygen content (30–50 wt. % depending on the wood source) [1–3]. Liquid-phase hydrodeoxygenation (HDO) has been studied during the last few decades with the purpose of removing oxygen heteroatoms from lignocellulosic bio-oils. HDO is an exothermic process by which oxygen present in bio-oil components reacts with hydrogen over a catalyst resulting in water and a pool of hydrocarbons chemically similar to crude oil [4–7]. High pressures are used to ensure proper solubility of hydrogen in bio-oils, as well as to increase its availability in the vicinity of the catalyst [7]. The process temperature is chosen taking into account that high temperatures may lead to catalyst deactivation, apparently caused by the large variability in activation energies of the different bio-oil constituents during HDO [7].

Conventional hydrotreating catalysts (such as Co-MoS<sub>2</sub>/Al<sub>2</sub>O<sub>3</sub> and Ni-MoS<sub>2</sub>/Al<sub>2</sub>O<sub>3</sub>) as well as new catalysts based on transition (such as Cr, Mo, Nb, Ni, Ta, V and W) and noble metals (such as Pt, Pd, Rh and Ru)

have been extensively tested in hydrodeoxygenation of bio-oils [5–8]. On one hand, conventional hydrotreating catalysts are usually supported on alumina which it is transformed to bohemite in the presence of water. These catalysts also deactivate due to significant coke deposition. In addition, conventional sulfided catalysts poison the product oil with sulphur and suffer from deactivation due to the instability of the support sulfide phase. On the other hand, noble metal catalysts have high activity and stability, but they are too expensive and present high hydrogenation activity leading to excessive hydrogen consumption [6,7,9].

Other metal based catalysts supported on metal oxides (such as TiO<sub>2</sub>, ZrO<sub>2</sub>, CeO<sub>2</sub> and SiO<sub>2</sub>) and zeolites (such as ZSM-5, HZSM-5, MZ-5, HY and H-beta) have been tested, but they usually deactivate due to excessive acidity of these supports which result in catalyst coking [4,6,10]. Therefore, the research on affordable, active, selective and reusable HDO catalysts is a research topic of great interest.

Transition metal carbides have recently received increased attention as their properties resemble those of noble metal catalysts [11,12] and have shown to be effective catalysts for hydrogenolysis, hydrogenation, isomerization reactions, as well as electrocatalytic hydrogen evolution and HDO of biomass derived oxygenates, as recently reviewed in [12]. The introduction of carbon in the lattice of transition metals leads to an increase in the lattice constant, which leads to a contraction of the d-band. Through carburization the d-electron density of transition metals

\* Corresponding author.

E-mail address: [jlpinilla@icb.csic.es](mailto:jlpinilla@icb.csic.es) (J.L. Pinilla).

<https://doi.org/10.1016/j.apcatb.2018.08.043>

Received 7 May 2018; Received in revised form 1 August 2018; Accepted 17 August 2018

Available online 18 August 2018

0926-3373/ © 2018 Elsevier B.V. All rights reserved.

increases at the Fermi level, conferring to the parent metal an electron density similar to those of noble metals; and the higher the carbon content of the obtained materials, the higher the noble metal-like behavior [13–15]. Density functional theory studies have revealed that Mo<sub>2</sub>C are particular suitable for heterogeneous catalyzed reactions where electron transfer is needed from the catalyst to the adsorbed reactant, characteristic of bond breaking reactions such as HDO [16,17].

The use of high-surface area supports allows to stabilize highly dispersed carbide nanoparticles, thus overcoming the drawbacks associated to the small surface area of the native Mo<sub>2</sub>C [18]. In the case of carbon-based support materials, an additional advantage is that they can also serve as a carbon source for carburization, and H<sub>2</sub> can be used as carburization agent, being this method known as carbothermal hydrogen reduction (CHR) [19,20]. This avoids the use of hydrocarbons during the carburization stage, which may promote the formation of passivating carbon deposits on the catalytically active carbide surface [21].

Carbon-supported molybdenum carbides have been used in a number of reactions, such as HDO of bio-oils model compounds [22–29] and vegetable oils [23,24,30–33], dehydrogenation of methylcyclohexane [18], hydrodesulphurization of dibenzothiophene [33], hydrodenitrogenation of indole [34], deoxygenation or hydrogenation of guaiacol [28,35], lignin ethanolysis [36], H<sub>2</sub> production by hydrazine [37] or ethanol decomposition [38], steam reforming of methanol [21,39] and as electrocatalyst in hydrogen evolution reactions [32,40].

Among the different carbonaceous materials used as Mo<sub>2</sub>C supports, activated carbons (AC) are the most widely used [19,24–26,28,30,31,35,36,41–43], although other materials such as carbon blacks (CB) [32,34,44], multi-walled carbon nanotubes (MWCNT) [18,21,25,32,38,39,45,46], carbon nanofibers (CNF) [25,29,47,48] and ordered mesoporous carbons (OMC) [30,37] have also been tested.

Several parameters are involved in the carburization step, namely the carbon source, Mo loading, maximum carburization temperature, heating rate and carburization time, and all these variables are inter-related [44]. By changing these parameters is possible to tailor the Mo phases obtained after the carburization process. The formation of the  $\beta$ -Mo<sub>2</sub>C phase, obtained at 900–1000 °C using an inert gas (N<sub>2</sub> or Ar) during the carburization process [47,48], can be achieved at lower carburization temperatures using a flow of H<sub>2</sub> (600–800 °C depending on the carbon support) [18,23,31,41,44]. The effect of the carburization parameters during the CHR using carbon supports as the carbon source and H<sub>2</sub> as carburization gas is mainly focused on the effect of the temperature, although this variable was shown to be dependent on the Mo loading [44]. As a general rule, higher carburization temperatures resulted in higher Mo contents (as a result of higher burn-off of the support) and larger Mo<sub>2</sub>C crystallite sizes [18,23,41,44,49]. The latter has recently proven beneficial towards deoxygenation reactions [50]. Wang et al. studied the effect of the carburization temperature between 650 and 800 °C using an AC as catalytic support [23]. They found that the degree of crystallization of Mo<sub>2</sub>C and the Mo loading increased with increased CHR temperature, but BET surface area significantly decreased at temperatures higher than 650 °C. Best results in the HDO of 4-methylphenol were obtained when the catalyst was carburized at 650 °C. Therefore, it can be inferred that a compromise between the formation of the carbide phase and the weight loss due to carbon consumption and the loss of the textural properties of the catalyst must be found. Nonetheless, other parameters such as the heating rate and the holding time at the maximum carburization temperature also may impact on the morphology of the resulting catalyst. For instance, Guil-Lopez et al. reported that when the heating rate was reduced from 10 to 1 °C/min, the carburization step was favoured and it resulted in larger Mo<sub>2</sub>C crystallite sizes [44]. The authors claimed as the main cause the sintering of the carbide phase due to the prolonged exposure to the

carburization gas as a consequence of the lower heating rate and the relatively high maximum carburization temperature (840 °C). Pielaszek et al. studied the effect of the holding time (2 and 24 h) during carburization at 600 °C, observing a significant increase of the Mo<sub>2</sub>C crystallite size (from 8 to 14 nm) [43]. From this brief bibliographic review, it is clear that the CHR parameters play a paramount role on the development of carbon supported Mo<sub>2</sub>C catalysts, although their impact on the catalytic behaviour has been scarcely reported.

In this work, the preparation of catalysts based on molybdenum carbides supported on CNF was studied, emphasizing the formation of the carbide phase during the carburization process. The synthesis of Mo<sub>2</sub>C/CNF catalyst was performed by carburization of ammonium heptamolybdate under H<sub>2</sub> flow and using CNF as carbon source. CNF has a crucial role in the catalyst synthesis aside from support purpose. Thus, two different parameters were studied in the catalyst carburization process, namely, the temperature and the heating rate. Then, the performance of the prepared catalysts was jointly evaluated in the HDO of guaiacol. Liquid products of the guaiacol HDO were identified and quantified by gas chromatography and the guaiacol conversion, product yields and HDO ratio of each catalyst were established.

## 2. Experimental

### 2.1. CNF synthesis and functionalization

CNF were produced by synthetic biogas decomposition (CH<sub>4</sub>:CO<sub>2</sub>; 50:50 v/v) over a Ni:Co:Al catalyst (33.5:33.5:33; wt. %). Decomposition was conducted in a rotary bed reactor at 650 °C using a weight hourly space velocity of 30 L<sub>N</sub>/(g<sub>cat</sub> h). As-produced CNF were purified by sonication with HCl (37%) at 60 °C during 4 h, followed by a functionalization step with HNO<sub>3</sub> (65%) at boiling point during 1 h [51]. After each step nanofibers were filtered (Whatman® cellulose filter; 0.2  $\mu$ m), rinsed with distilled water until pH = 7, and dried at 80 °C overnight. The final material was denoted as CNF. The purification treatment aimed to remove the catalyst trapped in the CNF, while the functionalization treatment intended for creating oxygen groups over the nanofiber surface and facilitating the subsequent metal dispersion, as detailed in previous works [52,53].

### 2.2. Synthesis of Mo<sub>2</sub>C catalysts

Mo<sub>2</sub>C catalysts were prepared by incipient wetness impregnation followed by a carburization stage with H<sub>2</sub> as carburization agent (CHR) [23,50,54]. Purified CNF were impregnated with an aqueous solution of ammonium heptamolybdate tetrahydrate ((NH<sub>4</sub>)<sub>6</sub>Mo<sub>7</sub>O<sub>24</sub>·4H<sub>2</sub>O) and dried at 60 °C (impregnated material is called as AHM/CNF herein-after). The amount of impregnated AHM was calculated for a Mo loading of 10 wt. % after carburization. CNF/AHM were carburized in a fixed-bed quartz reactor under a stream of H<sub>2</sub> (100 mL/min) at different heating ramps (1, 2.5, 5 and 10 °C/min) and operating temperatures (550, 600, 650, 700 and 750 °C). Once reached the carburized temperature, the material was maintained for 1 h at the desired temperature, and then cooled to room temperature under pure N<sub>2</sub> flow. Then, the catalysts were passivated for 1 h using a flow of 1 vol. % O<sub>2</sub> in N<sub>2</sub> at room temperature and store until use.

### 2.3. Experimental facilities and HDO tests

The effects of carburization temperature and heating rate on the conversion of guaiacol, product yield and HDO ratio were calculated as follows:

Conversion (%) = [(initial moles of guaiacol in feed - moles of guaiacol in product)/initial moles of guaiacol in feed]  $\times$  100

Yield (%) = (total moles of product/initial moles of guaiacol in feed)

× 100

HDO ratio (%) = [(initial moles of oxygen in feed - moles of oxygen in product)/initial moles of oxygen in feed] × 100

Moles of O in product =  $\sum \frac{\text{moles of product}}{\text{number of O atoms in the product}}$

The catalytic tests were performed in a 100 mL batch autoclave reactor (Autoclave Engineers). The reactor was loaded with 1.2 mL of guaiacol, 40 mL of n-decane and 0.2 g of catalyst. The reactor was purged with pure N<sub>2</sub> (Air Liquid, 99.999%) and then loaded with pure H<sub>2</sub> (Air Liquid, 99.999%) until a pressure of 20 bar. Then the temperature was raised at the desired temperature a heating rate of 10 °C/min, and the final H<sub>2</sub> pressure achieved was 32 bar. HDO experiments were performed at 300 °C for 2 h. The activity of CNF was also performed in order to determine the support catalytic effect on the guaiacol HDO.

After each experiment, catalyst was separated by filtration (Whatman® cellulose filter; 0.2 µm), rinsed with 50 mL pure ethanol, and the filtrate was chemically analyzed aiming the detection of intermediate reaction compounds.

For the characterization of the liquid phase after HDO reaction a CLARUS 580 gas chromatograph (Perkin Elmer) equipped with a 30 m long and 250 µm diameter Elite-5 column (crossbond: 5% diphenyl-95% dimethylpolysiloxane). The sample was introduced to the oven employing a split ratio of 19/1 at 275 °C and measured by a flame ionization detector (FID) at 330 °C. He was employed as a carried gas to introduce the vaporized sample into the column, 40 °C was set at initial temperature, ramped to 275 °C by 5 °C/min to achieve a good peak separation, further ramped to 330 °C by 15 °C/min and held at it for 5 min to ensure the complete elution of all products presents in the sample.

Reaction products were identified in a Varian CP 3800 GC coupled with a Varian Saturn 2200 mass spectrometer (MS) by comparison with the spectrum found in the instrument library. The GC/MS was fitted with the same column as the GC-FID and operated using the same temperature program. Quantification of reaction products was performed by establishing GC response factors of cyclohexane, benzene, toluene, guaiacol, n-decane and catechol, by injection of known concentrations.

Tests to assess experimental repeatability and to determine random error were carried out (conversion standard deviation,  $\sigma = 0.033$ ).

#### 2.4. Characterization techniques

The carburization reaction was studied by thermogravimetric analysis (TGA) using  $10 \pm 1$  mg of CNF/AHM as starting material. The mass losses were recorded in a TG 209 F1 Libra (NETZSCH®) thermobalance under a flow of 50 mL/min of H<sub>2</sub>/He (10% v/v). Temperatures of 550, 600, 650, 700 and 750 °C were studied using a heating ramp of 10 °C/min. In addition, samples were kept at set point temperature during 10 h. The gases released during the carburization were qualitatively measured with an AutoChem Analyzer II 2920 (MICROMETRICS®) from room temperature to 1000 °C using a heating rate of 10 °C/min.

The textural properties of the support and the catalysts were measured by N<sub>2</sub>-physisorption at 77 K in a Micrometrics ASAP2020 apparatus. The specific surface area ( $S_{\text{BET}}$ ) was calculated by applying the BET method to the respective N<sub>2</sub> adsorption isotherm. The total pore volume ( $V_t$ ) was calculated at a relative pressure of  $P/P_0 > 0.994$ . Size pore distribution was obtained applying the BJH method to the desorption isotherm.

The crystallite size, phase composition and structure of final catalysts were studied by X-ray diffraction (XRD) employing a Bruker D8 Advance Series 2 diffractometer equipped with Ni-filtered  $\text{CuK}\alpha$

radiation and a secondary graphite monochromator. The scans were performed using a range of 20–80° each 0.05° every 3 s. The crystal size was processed using DIFRAC PLUS EVA 8.0 and TOPAS software.

X-ray photoelectron spectroscopy (XPS) patterns were obtained in an ESCAPlus (OMICRON) spectrometer equipped with a hemispherical electron energy analyzer. X-ray was operated at 225 W (15 mA and 15 KV) using a non-monochromatized MgAl $\alpha$  ( $h\nu = 1486.7$  eV) under vacuum ( $< 5 \times 10^{-9}$  Torr). Deconvolutions and processing of XPS spectra were performed by CASA XPS software using Shirley type background, peak fitting, identification and quantification.

The metal composition of catalysts was obtained by inductively coupled plasma optical emission spectrometry (ICP-EOS); the sample was prepared by sodium peroxide fusion procedure and introduced to Spectroblue (AMETEK) for the quantification.

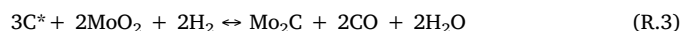
The morphology of catalysts was observed by transmission electron microscope (TEM) and scanning transmission electron microscope (STEM) techniques. TEM and STEM images were captured using JELO-2000 FXII microscope operating at 200 KeV equipped with EDX and Tecnai F30 (FEI) at 300 KeV, respectively. For both techniques, samples were supported in a copper grids covered with a lacey amorphous carbon film.

### 3. Results and discussion

#### 3.1. Effect of the carburization temperature on the HDO of guaiacol

CNF used as catalysts support showed fishbone-type morphology (see Figs. S1 and S2 in the Supplementary Information), with an average outer diameter around 30 nm and the presence of an inner hollow, opened at its ends as consequence of metal removal after the purification and oxidation treatments. In addition, a  $S_{\text{BET}}$  of 98.7 m<sup>2</sup>/g and a  $V_t$  of 0.392 m<sup>3</sup>/g were measured by N<sub>2</sub> physisorption for the purified CNF, whose pore distribution (see Fig. S3 in the Supplementary Information) showed the presence of micropores, related to the free internal volume and the wall roughness of the nanofibers, and mesopores, centered on 30 nm and due to the crosslink of the nanofilaments.

CNF were impregnated with AHM (CNF/AHM) and carburized under an H<sub>2</sub>/He (10% v/v) flow in thermobalance at different temperatures. This technique allows to outline the weight changes suffered by the sample during the carburization process. TGA carried out at different carburization temperatures in the range 550–750 °C and the differential thermogravimetry (DTG) curve of the analysis at 750 °C are shown in Fig. 1a and b, respectively. According to TGA curves, three zones of mass loss were delimited, which are related to three different reduction stages [18,21,50]: Zone I corresponds to the degradation of AHM into MoO<sub>3</sub> (around 204 °C; reaction R.1); Zone II shows the reduction of MoO<sub>3</sub> into MoO<sub>2</sub> (200–560 °C) that presents a maximum at 468 °C (reaction R.2); and Zone III is related to the transformation of MoO<sub>2</sub> into Mo<sub>2</sub>C (560–750 °C) showing a maximum at 686 °C (reaction R.3).



The TGA performed below 650 °C (500 and 600 °C) only reached the two first mass loss zones, indicating that AHM was completely transformed into MoO<sub>2</sub>. A further increase in the final temperature allowed to complete the carburization of MoO<sub>2</sub> into Mo<sub>2</sub>C. To confirm this, AHM/CNF sample was carburized from room temperature up to 1000 °C in a thermobalance coupled with MS. The composition of the gas stream produced during the test is shown in Fig. 2. A small contribution of CO<sub>2</sub> ( $m/z = 44$ ) was also detected due to the reduction of oxygenated functional groups created during the functionalization of CNF. NH<sub>3</sub> signal ( $m/z = 17$ ) was related to the decomposition of AHM

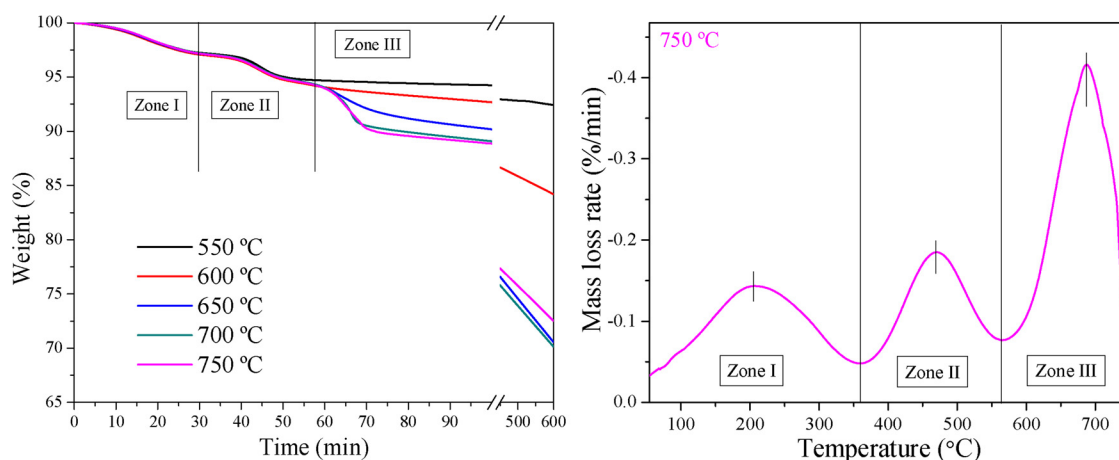


Fig. 1. TGA profiles of CNF/AHM: a) loss mass registered over time at five different temperatures; b) DTG profile of the sample carburized at 750 °C.

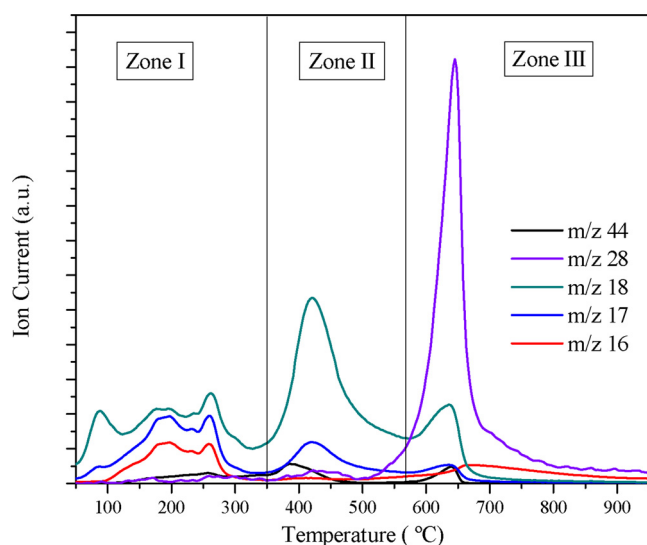


Fig. 2. MS profiles of CNF/AHM during carburization.

to  $\text{MoO}_3$  [55], and it was detected in the 100–300 °C interval. A small  $m/z = 17$  peak detected at ca. 425 °C is attributed to OH fragments from  $m/z = 18$  and therefore can be considered a secondary signal of water [56]. CO signal ( $m/z = 28$ ) started around 500 °C and showed a maximum at 645 °C. CO was related to the transformation of  $\text{MoO}_2$  to  $\text{Mo}_2\text{C}$ , and it was accompanied with the formation of  $\text{H}_2\text{O}$  ( $m/z = 18$ ), according to the reaction R.3 [41].  $\text{H}_2\text{O}$  signal ( $m/z = 18$ ) showed four peaks: a first peak at 80–200 °C related to the sample moisture, and three remaining peaks related to the three reduction zones mentioned above. Besides,  $\text{CH}_4$  signal ( $m/z = 16$ ) detected was produced by the gasification of the support catalyzed by  $\text{Mo}_2\text{C}$  [21,23,41,57]. Due to carbon gasification, a progressive mass loss at high temperature and operating time was recorded by TGA (Fig. 1a). At 550 and 600 °C, the weight loss after 10 h was less than those obtained at temperatures at which  $\text{Mo}_2\text{C}$  was formed. The degree of gasification was determined from the weight loss measured during the CHR of the AHM/CNF samples (discounting from the total weight loss the weight loss associated to the transformation of AHM into  $\text{Mo}_2\text{C}$ ) (Supporting Information, Table S1), confirming that it increased as the carburization temperature did.

The XRD patterns of catalysts obtained after carburization carried out in a fixed-bed quartz reactor for 1 h (to minimize the gasification effect) are shown in Fig. 3. Catalysts showed the characteristic reflections of the planes: (002), (100), (101), (004) and (110) of the graphite phase of the CNF [58]. The diffractograms also showed reflections attributed to the molybdenum carbide ( $\beta\text{-Mo}_2\text{C}$ ) and molybdenum oxide

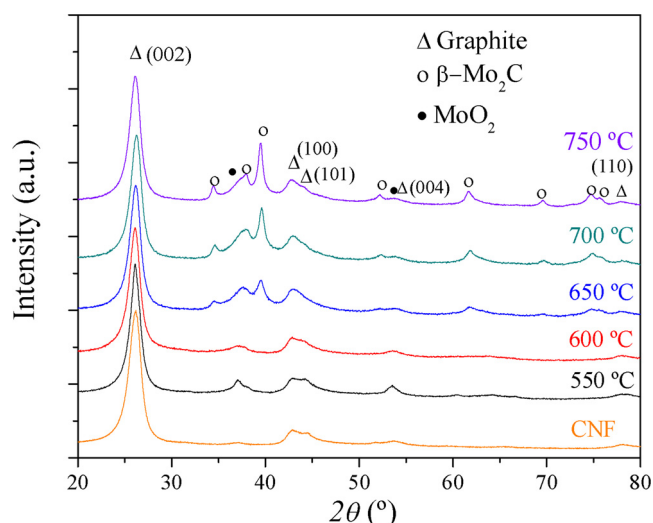


Fig. 3. XRD patterns for the catalysts carburized at different temperatures using a heating rate of 1 °C/min and held on set point for 1 h.

( $\text{MoO}_2$ ) phases [28].  $\text{Mo}_2\text{C}$  reflections detected correspond to the  $\beta\text{-Mo}_2\text{C}$  phase (hcp structure) with its most intensive peak at 39.4° [59]. XRD patterns showed the  $\text{MoO}_2$  transformation during the carburization process as a function of the operating temperature, while  $\beta\text{-Mo}_2\text{C}$  phase was only detected at temperatures above 650 °C. Catalysts carburized at temperatures over 650 °C showed a decrease on the intensity of  $\text{MoO}_2$  signal and an increase of  $\beta\text{-Mo}_2\text{C}$  peaks, indicating larger  $\beta\text{-Mo}_2\text{C}$  crystals (see Table 1). Thus, the  $\beta\text{-Mo}_2\text{C}$  crystal size increased from 6.7 to 10.9 nm as the carburization temperature was raised from 650 to 750 °C. The Mo content in the catalysts was in the range

Table 1

Crystal sizes of molybdenum carbide and oxide and molybdenum amount determined by XRD and ICP-OES, respectively, for catalysts carburized at different temperatures.

Carburization temperature (°C)	XRD		ICP-OES Mo (wt. %)	N <sub>2</sub> physisorption	
	$\beta\text{-Mo}_2\text{C}$ (nm)	$\text{MoO}_2$ (nm)		$S_{\text{BET}}$ (m <sup>2</sup> /g)	$V_t$ (m <sup>3</sup> /g)
550	–	4.3	10.0	57.4	0.362
600	–	2.7	10.3	56.2	0.352
650	6.7	2.5	11.6	65.1	0.395
700	9.1	2.0	12.4	62.0	0.353
750	10.9	2.0	12.9	64.2	0.398



10.0–12.9 wt. % according to the ICP-OES analyses (Table 1). Previous works showed that carbonaceous supports may suffer gasification during the carburization process at relatively high temperatures [23,41], as discussed above (see Fig. 1). In this work the carbon gasification started from 525 °C, so the catalysts carburized at 550 °C presented a Mo content close to the nominal (10 wt. %), while the catalysts carburized at higher temperatures showed a slightly higher Mo content (around 12 wt. %) due to the gasification of the support.

After the carburization, the  $S_{\text{BET}}$  of the catalysts was determined by  $\text{N}_2$  physisorption (Table 1). These results highlighted the loss of  $S_{\text{BET}}$  with respect to that presented by the CNF before carburization and impregnation (98.7  $\text{m}^2/\text{g}$ ). The loss in  $S_{\text{BET}}$  has been already observed in the carburization process using an AC as support/carbon precursor [23]. However, the catalysts carburized at lower temperatures (550 and 600 °C) showed  $S_{\text{BET}}$  around 56–57  $\text{m}^2/\text{g}$ , slightly lower than those presented by the sample carburized at higher temperatures (650 °C and above) which were around 62–65  $\text{m}^2/\text{g}$ . Such increase, despite the disappearance of the support into the  $\beta\text{-Mo}_2\text{C}$  phase, might be due to a slight support gasification which promotes the formation of defects and exposes internal surfaces of the carbon nanofibers. On the other hand, the  $V_t$  of the catalysts ranged from 0.352 to 0.398  $\text{m}^3/\text{g}$ , and their pore size distributions were similar to that of the starting CNF (see Fig. S3 in the Supplementary Information).

In order to determine the Mo surface content and oxidation state of the carburized samples, XPS analyses were performed. The deconvolution of the Mo3d XPS region and the survey composition of catalysts carburized at different temperatures are shown in Fig. 4 and Table 2, respectively. The surface Mo content determined by XPS and the Mo/C ratio increased with the carburization temperature, indicating a better Mo dispersion and thus higher amount of available Mo active sites. As for the Mo3d deconvolution, all catalysts showed four components related to different Mo oxidation states:  $\text{Mo}^{2+}$  (227.5–228.4 eV),  $\text{Mo}^{\delta+}$  (229.3 eV),  $\text{Mo}^{4+}$  (230.1–230.4 eV) and  $\text{Mo}^{6+}$  (232.5–232.9 eV).  $\text{Mo}^0$  (227.0  $\pm$  0.1 eV) was not observed in any case.  $\text{Mo}^{\delta+}$  state ( $2+ < \delta+ < 4+$ ) corresponds to an intermediate between the  $\text{Mo}_2\text{O}$  ( $\text{Mo}^{4+}$ ) and  $\beta\text{-Mo}_2\text{C}$  ( $\text{Mo}^{2+}$ ) phases and was attributed to the existence of a Mo oxycarbide phase [23,60]. Although catalysts carburized at 700 and 750 °C showed similar Mo/C ratio, the latter had a higher  $\text{Mo}^{2+}$  concentration. The XPS results were in accordance with those of XRD and TGA as they confirmed that a higher  $\beta\text{-Mo}_2\text{C}$  percentage was obtained at higher carburization temperatures. Nevertheless, a small amount of  $\beta\text{-Mo}_2\text{C}$  for the catalysts carburized below 650 °C was

identified.

In conclusion, the  $\text{MoO}_2$  carburization process using CNF as carbon source started around 550 °C, although it was not transformed directly into  $\beta\text{-Mo}_2\text{C}$ , but instead passed through the formation of an oxycarbide phase as intermediate state, which started to reduce to  $\beta\text{-Mo}_2\text{C}$  beyond 650 °C. Thus, the catalysts carburized at 550, 600 and 650 °C mainly contained  $\text{MoO}_2$  and the Mo oxycarbide phases, while the catalysts carburized at higher temperatures contained a mixture of both Mo oxycarbide and  $\beta\text{-Mo}_2\text{C}$  phases.  $\text{Mo}^{6+}$ , ascribed to the  $\text{MoO}_3$  phase, was attributed to the passivation performed after the carburization process, the reason why it was detected in all the catalysts synthesized for this work. The removal of this passivation layer using an Ar sputtering pretreatment before the XPS measurement was discarded due to the secondary formation of  $\beta\text{-Mo}_2\text{C}$  phase, as previously reported [61] (see Fig. S4 in the Supplementary Information).

Regarding the microscopy analysis, TEM and STEM images are shown in Figs. 5 and 6, respectively. Samples showed, independently of the carburization temperature used in the synthesis, molybdenum particles (darker zones in the TEM image) of different sizes and shapes both covering the outer surface and in the inner hollow of the carbon nanofiber (this can be easily clearly observed in Fig. 5b, d and f). It is thus confirmed that the molybdenum precursor also impregnated the nucleus of the carbon nanofiber, a location that seemed to favor the formation of larger and more carburized particles than those observed on the outer surface. High-temperature carburized catalysts showed darker (high crystallinity) and more spherical particles of ca. 10 nm (Fig. 5f) than those observed on catalysts carburized at lower temperatures (Fig. 5b and d), over which flake shape, less crystalline (less dark on TEM images) larger particles were observed. At a carburization of 700 °C (see Fig. S5 in the Supplementary Information), no morphological differences were observed with respect to the TEM images of catalysts carburized at 750 °C. In addition, very small nanoparticles (< 2 nm) were perceived by HRTEM evenly covering the CNF for the catalysts carburized at higher temperatures: 650 and 750 °C (see circles in Fig. 5c and e). These nanoparticles were better resolved by STEM, where the small particles (bright spots) were clearly observed coating the surface of all catalysts (Fig. 6a, c and e), even on the catalyst carburized at 550 °C whose nanoparticles were barely observed by TEM due to the less compact structure of the molybdenum oxide (Fig. 5a). The brightness of those small spherical nanoparticles was attributed to their metallic composition which corresponded to molybdenum-based phases (oxide, oxycarbide or carbide). Like by TEM, differences were also found by this technique: brighter and spherical particles were observed over catalysts carburized at high carburization temperatures (Fig. 6f), contrasting with less brighter and elongated particles detected over catalysts at lower temperatures (Fig. 6b and d). EDX of some representative samples (Fig. S6 in Supporting Information) confirmed the presence of Mo particles either inside the tube cavities or in the outer walls of the CNF.

The catalyst's performance was studied in the HDO of guaiacol at 300 °C and 20 bar of  $\text{H}_2$  (initial pressure at room temperature). Guaiacol conversion, yields to products and HDO ratio obtained of the catalysts carburized at different temperatures are shown in Fig. 7. For comparison reasons, the catalytic performance of the CNF support was measured separately in the HDO of guaiacol, achieving a 10.0% of conversion after 2 h of reaction. The liquid phase yields determined by GC were: phenol (0.6 wt. %), catechol (0.7 wt. %) and toluene as the main product (3.8 wt. %). Others, such as volatiles and cracking products were determined by difference (4.9 wt. %). The production of toluene from guaiacol over the bare CNF support can occur by three reaction pathways: 1) partial deoxygenation of guaiacol to cresols followed by dehydroxylation to toluene, 2) dehydroxylation of guaiacol followed by deoxygenation to toluene or 3) simultaneous deoxygenation and dehydroxylation of guaiacol to toluene [62,63]. Since no cresols or anisole (intermediate products) were detected by GC–MS, two scenarios seem possible: 1) the intermediate reactions were very fast this way

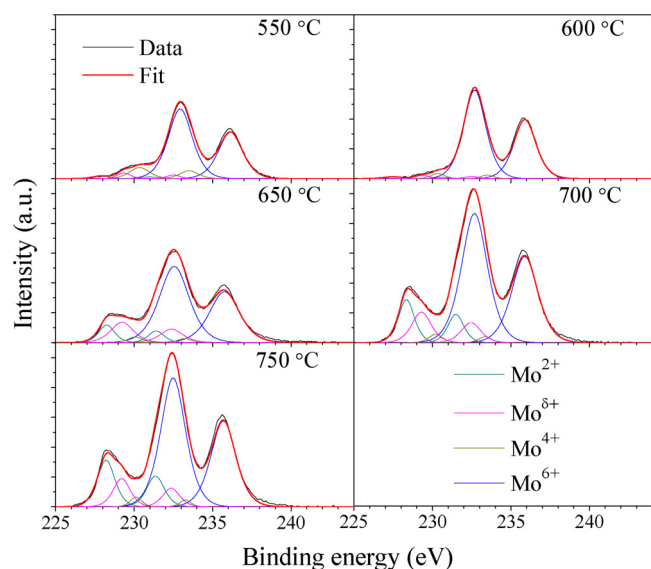
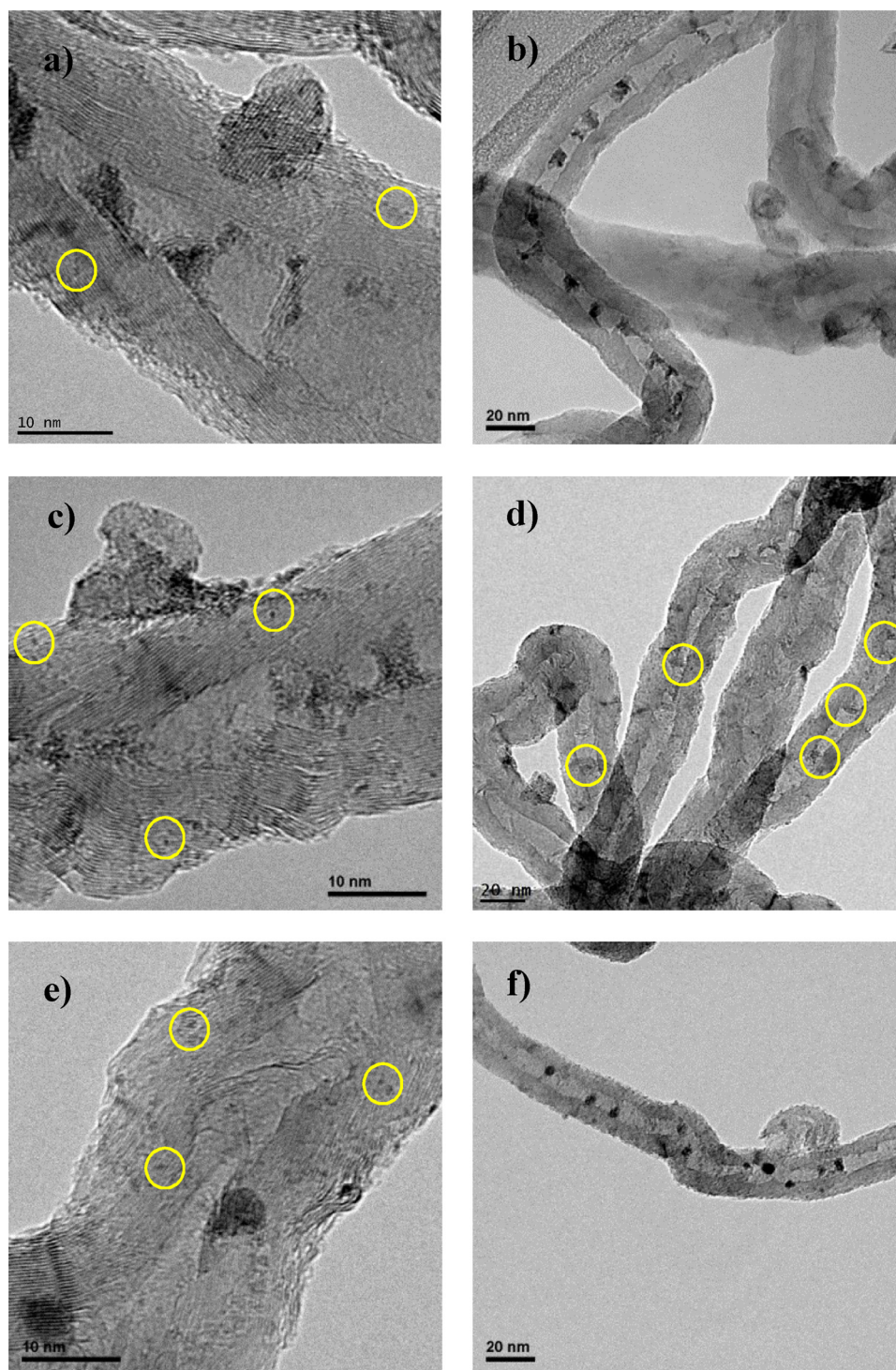


Fig. 4. Deconvolution of Mo3d XPS spectra for catalysts carburized at different temperatures. Carburization carried out in the fixed-bed quartz reactor.

**Table 2**

Molybdenum oxidation state and atomic composition determined by XPS for catalysts carburized at different temperatures.

Carburization temperature (°C)	Mo species (at. %)				Composition (at. %)			Mo/C
	Mo <sup>2+</sup>	Mo <sup>δ+</sup>	Mo <sup>4+</sup>	Mo <sup>6+</sup>	Mo	O	C	
550	2.3	3.7	10.9	83.2	1.0	3.2	95.8	0.010
600	1.7	2.2	3.3	92.9	1.0	2.7	96.4	0.010
650	6.0	18.6	2.4	73.0	1.5	4.3	94.2	0.016
700	14.8	12.5	2.1	70.6	2.4	5.2	92.4	0.026
750	17.7	10.4	2.4	69.5	2.3	5.1	92.7	0.025

**Fig. 5.** HRTEM images of catalysts carburized at: (a,b) 550 °C, (c,d) 600 °C and (e,f) 750 °C.



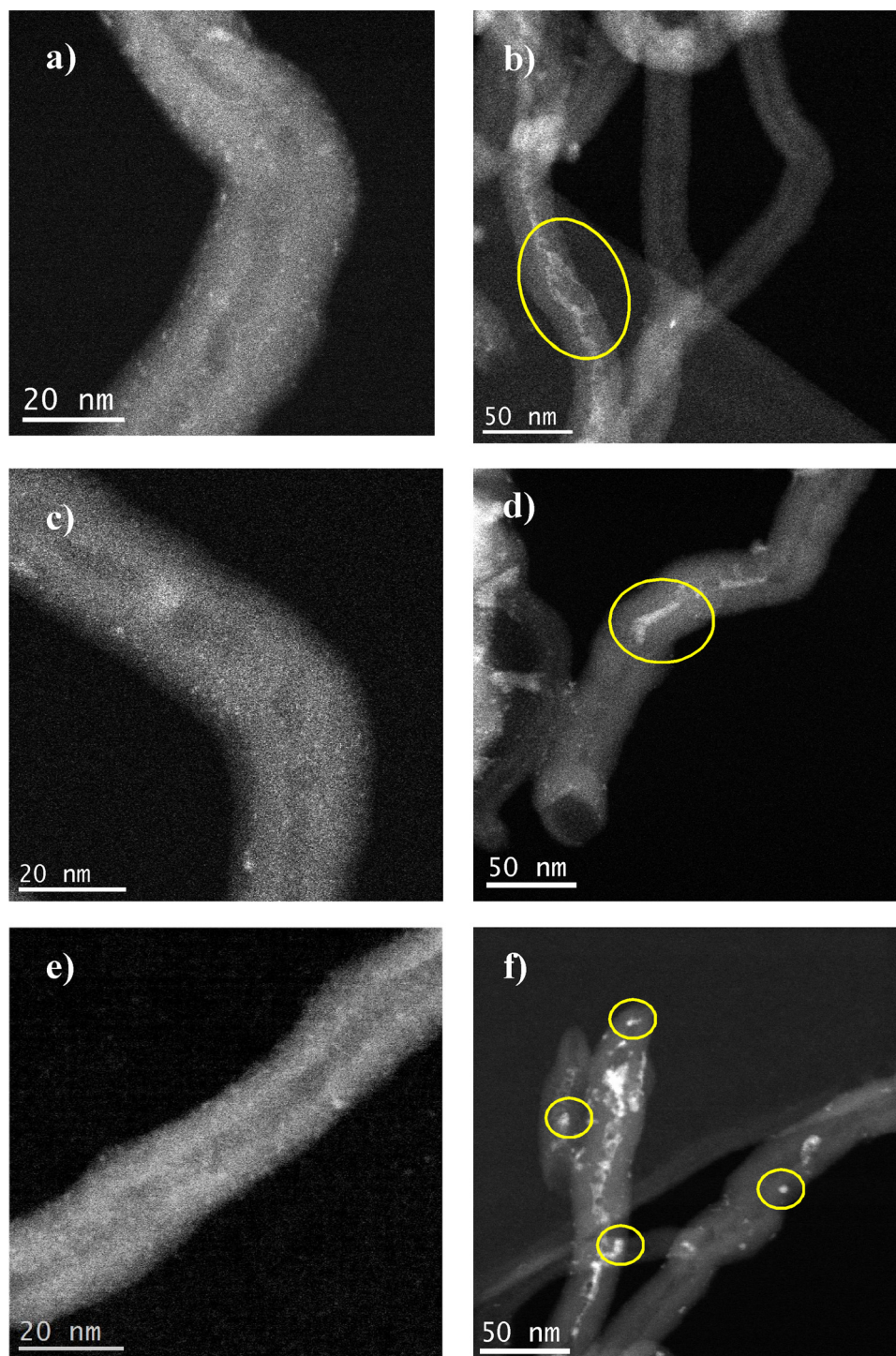


Fig. 6. STEM images of catalysts carburized at: (a,b) 550 °C, (c,d) 600 °C and (e,f) 750 °C.

explaining the non-detection of intermediate products (cresols or anisole) or 2) the conversion of guaiacol was low allowing for the full conversion of intermediate products to toluene. Following this train of thinking, the results indicate that intermediate products (cresols or anisole) were fully converted into toluene, since the conversion of guaiacol into liquid products was only 5.1%. However, the possibility of simultaneous deoxygenation and dehydroxylation of guaiacol to toluene cannot be fully discarded. In fact, it is known simultaneous dehydration-decarboxylation reactions can occur over acidic zeolites [62]. By the evolution of CO<sub>2</sub> during TPD analysis, the existence of acid sites over the bare CNF support was demonstrated, which could have

catalyzed the conversion of guaiacol into toluene. The low acidity of such sites may justify the corresponding low overall conversion (10%). In catalytic experiments involving the Mo catalysts, the conversion obtained increased and the final products changed drastically. The catalytic activity increased as the carburization temperature did, presumably due to the increase in the  $\beta$ -Mo<sub>2</sub>C size and its concentration in the catalyst as previously shown by XRD and XPS, respectively. This resulted in the increase in the number and quality of  $\beta$ -Mo<sub>2</sub>C noble-metal like sites [15]. In order to take into account the relatively small differences in Mo content (between 10 and 13 wt. %, as shown in Table 1), we have normalized the guaiacol conversion and the

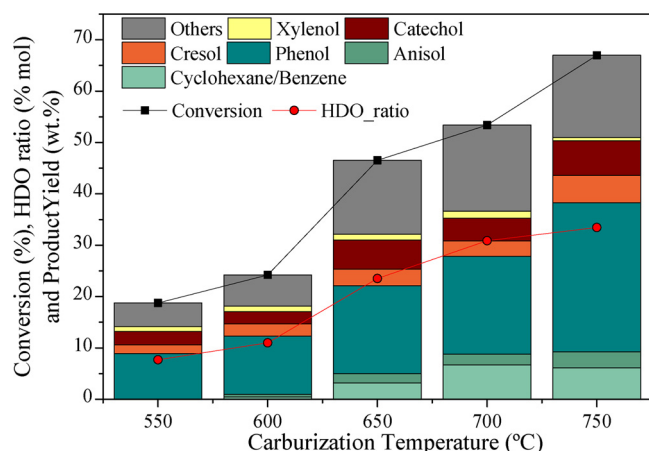


Fig. 7. Guaiacol conversion, yields to products and HDO ratio for the catalysts carburized at different temperatures. HDO: 300 °C, 20 bar of  $H_2$  and 2 h of reaction.

formation of partially deoxygenated products per amount of Mo present in the catalysts, as shown in Table S2 in the Supporting Information. These data confirmed the previous observation related to the superior catalytic activity of the catalyst carburized at the highest temperature.

Moreover, for all catalysts, phenol (8.9–29.0 wt. %) was the main product detected together with lower quantities of new products (not observed using the bare CNF support) such as *o*-cresol and *p*-cresols (denoted as cresols), anisole, cyclohexane and benzene. Soluble higher molecular weight products that could not be detected by GC were grouped as “others” [47], and calculated by the difference in mass balance (see Table S3 in Supporting Information). Carbon balance was also calculated and it typically closed between 88 and 95% (Table S3 in Supporting Information).

Considering the reaction products obtained in the liquid phase, different reaction pathways could be differentiated (Fig. 8): HDO reactions (HDO) and reactions of demethylation/methyl substitution of guaiacol and products (MET). MET product yields (catechol, xylenol and cresols) were in the range of 5.3–12.7 wt.%, while HDO product yields (cyclohexane + benzene, anisole and phenol) accounted for 8.9–38.2 wt. %, depending on catalyst carburization temperature.

The main products obtained using the developed Mo catalysts were HDO products such as phenol, anisole and benzene, while MET products (cresols, catechol and xylenol) were formed in much less amount, regardless of the carburization temperature. These results clearly pointed out that Mo based catalysts favoured the direct cleavage of Ar–OCH<sub>3</sub> bond rather than the removal of the phenolic group (Ar–OH), as previously reported for Mo<sub>2</sub>C [47] or MoO<sub>2</sub> based catalysts [22].

The formation of cyclohexane and benzene was achieved using catalysts carburized over 600 °C. These catalysts reached a successful carburization of AHM, showing a higher concentration of  $\beta$ -Mo<sub>2</sub>C at the

expense of the molybdenum oxycarbide phase transformation. Likewise, catalysts carburized at 550 °C also achieved higher selectivities to hydrodeoxygenated compounds than to MET products, indicating that molybdenum oxycarbide also presents HDO activity, but was lower than that of the  $\beta$ -Mo<sub>2</sub>C phase. In all cases, phenol was the main product obtained after HDO, and its yield increased with the carburization temperature of the catalysts. Phenol is a high value product produced at large scale in petroleum refineries, and is extensively used as precursor to obtain processed materials such as plastics, polymers, herbicides, cosmetics and pharmaceuticals, among others [64]. As MET products, catechol (2.3–6.7 wt. %), xylenol (0.6–1.3 wt. %) and cresols (2.3–5.3 wt. %) were obtained. Catechol has importance as chemical product used in the production of pesticides and as precursor of perfumes and drugs [65,66]. These results clearly showed the importance of reaching 650 °C during the carburization process in order to achieve  $\beta$ -Mo<sub>2</sub>C phase and exert the catalytic effect evidenced by the differences in product yields and conversion.

### 3.2. Effect of the carburization heating ramp on the HDO of guaiacol

Considering the results of previous section, a new set of catalysts was prepared using four different carburization heating rates (1, 2.5, 5 and 10 °C/min) and the carburization temperature at which the best behaviour in the guaiacol HDO was obtained (750 °C; see Fig. 7). Both the techniques used to characterize the catalysts and the operating conditions used in the HDO experiments were identical to those used in the previous section. Even though same crystallographic phases were detected at all tested heating rates (see Fig. 9), differences in the crystal sizes were observed. Crystal sizes measured by XRD are summarized in Table 3. Lower heating rates imply longer times until the set point temperature is reached, being thus the carburization more effective and larger the  $\beta$ -Mo<sub>2</sub>C formed. The carburization performed using 1 °C/min formed larger  $\beta$ -Mo<sub>2</sub>C crystals (10.9 nm) than those obtained using 10 °C/min (6.5 nm). Similar patterns and crystal sizes were obtained from the catalysts carburized employing faster heating rates (10 °C/min and 5 °C/min). Regarding ICP-OES results (Table 3), slightly higher molybdenum contents were obtained when the catalysts were carburized at lower heating rates. As mentioned in the previous section, catalysts suffered slight gasification during the carburization process (Fig. 1), which explains the differences on the Mo content. Thus, the catalyst carburized at low heating rates (1 and 2.5 °C/min), which implied longer gasification times, showed higher deviations from the nominal Mo content (10%).

As for the textural properties, similar  $S_{BET}$  (Table 3) were observed in catalysts carburized at different heating rates: the lowest  $S_{BET}$  (64.2 m<sup>2</sup>/g) was obtained for the slowest heating rate (1 °C/min). Likewise, no significant differences were found in their size porous distribution (see Figure S7 in the Supplementary Information).

The deconvolution of the Mo3d region of the catalyst XPS spectra and their atomic composition are shown in Fig. 10 and Table 4, respectively. Although the surface Mo content of this set of catalysts was

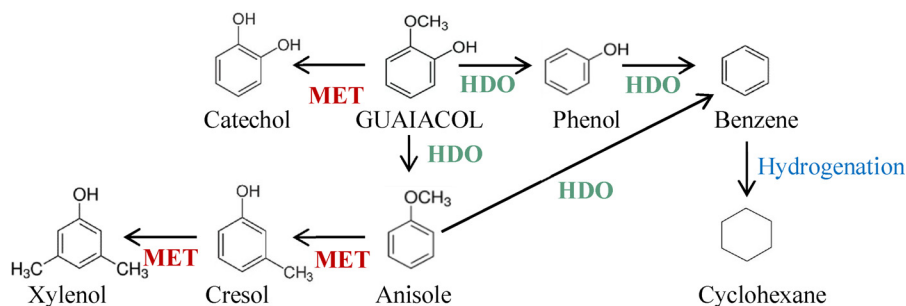


Fig. 8. Simplified scheme of the products obtained after HDO of guaiacol divided in: demethylation/methyl substitution products (MET) and hydrodeoxygenation products (HDO).



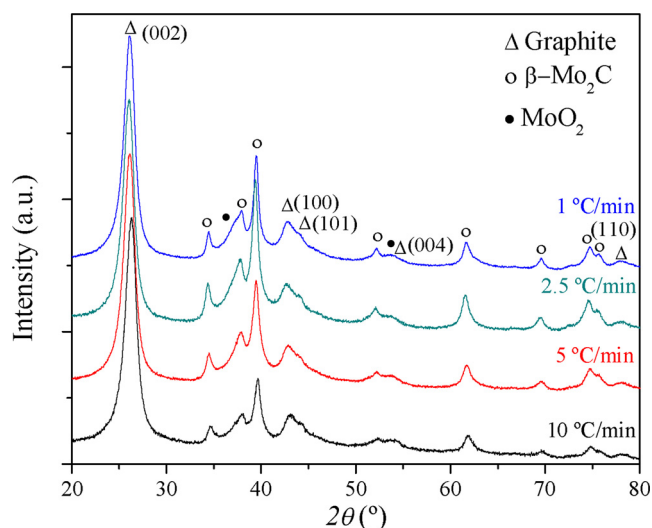


Fig. 9. XRD patterns for the catalysts carburized at 750 °C and different heating rates.

Table 3

XRD and ICP-OES results of the catalysts carburized at 750 °C and different heating rates.

Heating rate (°C/min)	XRD		ICP-OES	N <sub>2</sub> physisorption	
	β-Mo <sub>2</sub> C (nm)	MoO <sub>2</sub> (nm)		Mo (wt. %)	S <sub>BET</sub> (m <sup>2</sup> /g)
1	10.9	2.0	12.9	64.2	0.398
2.5	7.6	2.5	12.7	67.1	0.412
5	7.0	1.8	11.7	68.4	0.404
10	6.5	1.7	11.5	68.4	0.423

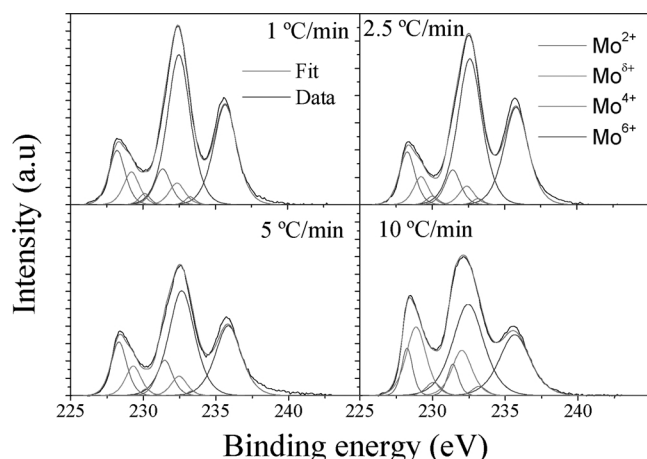


Fig. 10. Deconvolutions of Mo3d XPS spectra for the catalysts carburized at 750 °C and different heating rates.

Table 4

Molybdenum oxidation state and atomic composition calculated by XPS for the catalysts carburized at 750 °C and different heating rates.

Heating rate (°C/min)	Mo species (at. %)				Composition (at. %)			Mo/C
	Mo <sup>2+</sup>	Mo <sup>4+</sup>	Mo <sup>5+</sup>	Mo <sup>6+</sup>	Mo	O	C	
1	17.7	10.4	2.4	63.5	2.3	5.1	92.7	0.025
2.5	16.9	8.6	2.0	72.5	1.8	4.6	93.6	0.019
5	20.7	11.3	4.5	66.5	1.9	3.9	94.2	0.020
10	19.9	21.2	1.5	57.5	2.0	3.8	94.2	0.021

similar (around 2 at. %), the catalyst carburized using 1 °C/min obtained the highest value (2.3 at. %). This sample also showed the highest Mo/C ratio. The Mo oxidation state was determined by deconvolution of the Mo3d region of the XPS spectra in which all the catalysts showed Mo<sup>6+</sup> (MoO<sub>3</sub>) as result of passivation. However, the carbide phase was higher than the oxycarbide phase (Mo<sup>2+</sup> > Mo<sup>4+</sup>) for any heating rate employed. In addition, a small amount of Mo<sup>4+</sup> (MoO<sub>2</sub>) was identified.

The HRTEM images of the catalysts carburized at slowest (1 °C/min) and fastest (10 °C/min) heating rates can be found in Figure S8 (see Supplementary Information); however, no significant visual differences between the samples were found. Fig. 11 shows the STEM images taken to the catalysts carburized at 2.5 and 10 °C/min, revealing the existence of small Mo nanoparticles (lower than 2 nm) homogeneously covering the surface of the CNF.

Regarding the catalytic tests (Fig. 12), HDO products were formed in higher concentrations than MET products for all catalysts, being again phenol the main product obtained (18.0–38.2 wt.%). In these tests, carbon balance typically closed between 88 and 95% (Table S5 in Supporting Information). Cyclohexane and benzene were also obtained as final HDO products. Conversion and HDO ratios showed that an adequate crystal growth of β-Mo<sub>2</sub>C crystals (see Table 3) was attained by using low heating rates. These results were consistent with the characterization, since the catalysts carburized at heating rates of 2.5, 5 and 10 °C/min hardly showed differences in HDO product distribution. These three catalysts had similar Mo surface contents and β-Mo<sub>2</sub>C crystal sizes (around 7 nm); as consequence, they showed similar yields to HDO products and conversion. However, the catalyst carburized at 2.5 °C/min showed a higher guaiacol conversion (45%) than the other two, what was attributed to the slightly higher Mo content (as confirmed in Table S4 in the Supporting Information where the guaiacol conversion and the formation of deoxygenated products per amount of Mo present in the catalysts is shown) and the larger Mo<sub>2</sub>C crystal size obtained after carburization process (see Table 3).

The use of slower heating rates favoured the formation of larger β-Mo<sub>2</sub>C crystals that resulted in an improvement of the catalytic activity (Fig. 12 and Table S4 in the Supporting Information). Likewise, crystal sizes up to 10 nm showed the best catalytic behaviour (67% of guaiacol conversion and 55% HDO product yield), increasing the HDO ratio to 33%.

#### 4. Conclusions

Molybdenum carbide catalysts supported on carbon nanofibers (β-Mo<sub>2</sub>C/CNF) were synthesized employing different carburization temperatures and heating rates, and their behaviour in the HDO of guaiacol was tested.

- The carburization temperature had a direct effect on the formation of Mo carbides both in the content of this phase and in its crystallite size and structure. β-Mo<sub>2</sub>C was only obtained for catalysts where the carburization of ammonium heptamolybdate was carried out at temperatures above 650 °C, which showed higher catalytic activity in the HDO of guaiacol. Likewise, XPS revealed the existence of molybdenum oxycarbide as intermediate in the MoO<sub>2</sub> carburization into β-Mo<sub>2</sub>C. Both Mo species, oxide and oxycarbide, were in larger amounts in catalysts carburized at 550 and 600 °C, which showed a low catalytic behaviour in the HDO of guaiacol, reaching yields to HDO products and guaiacol conversions below 17 and 24%, respectively.
- The heating rate proved to be decisive in the β-Mo<sub>2</sub>C crystal size: slower heating rates formed larger crystallites; however, it had no influence on the Mo oxidation state, where β-Mo<sub>2</sub>C and Mo oxycarbide were the predominant phases detected by XPS. Hence, the catalyst carburized at the slowest heating rate showed the largest β-Mo<sub>2</sub>C crystallites (above 10 nm) and achieved the best catalytic

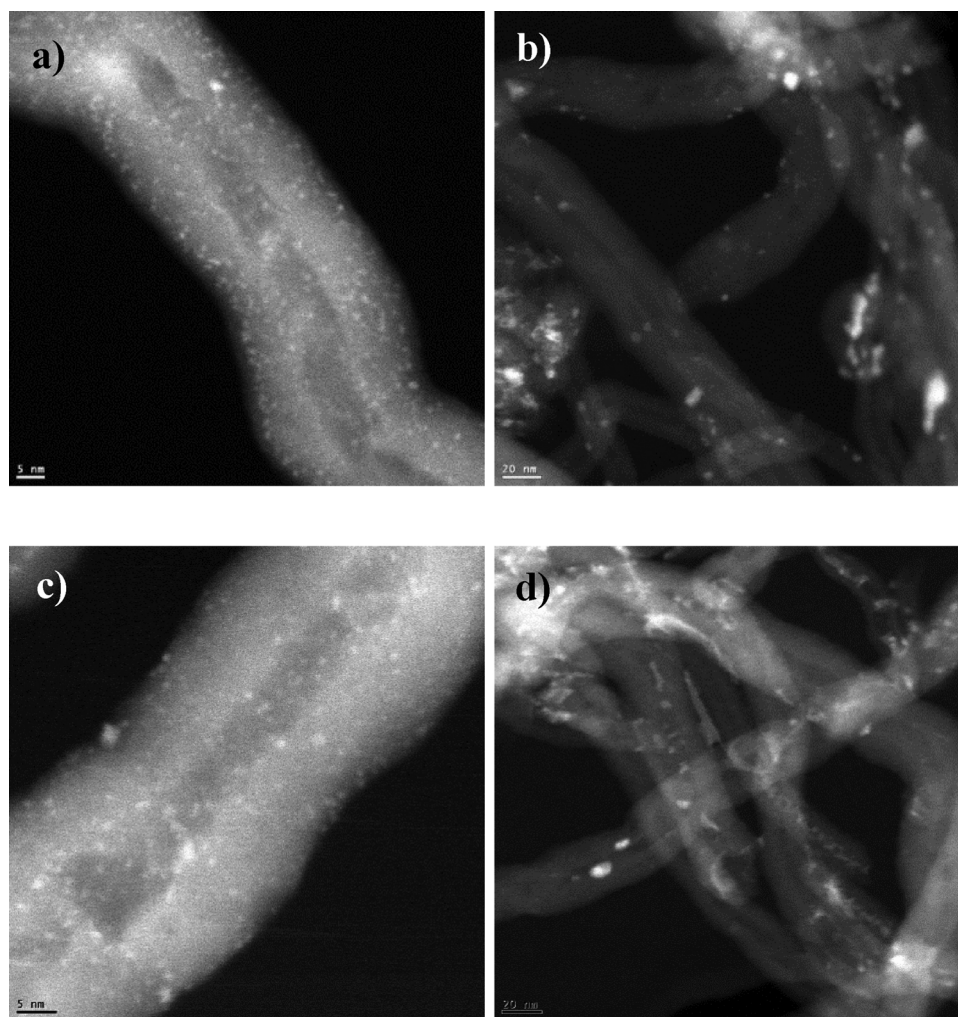


Fig. 11. STEM images of the catalyst carburized at 750 °C and different heating rates: (a,b) carburized at 10 °C/min and (c,d) at 1 °C/min.

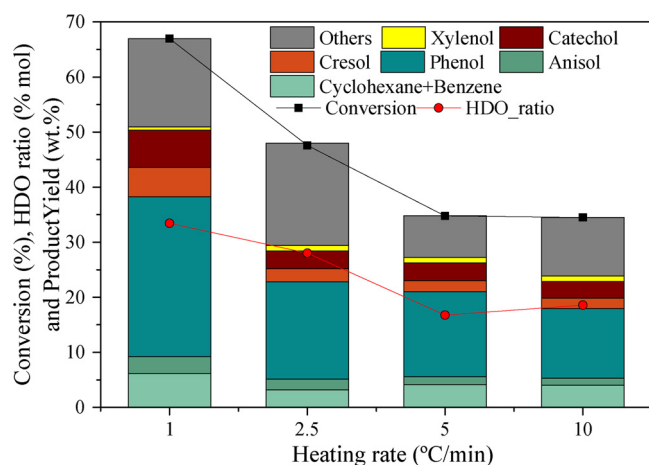


Fig. 12. Guaiacol conversion, yields to products and HDO ratio for the catalysts carburized at 750 °C and different heating rates. HDO: 300 °C, 20 bar of H<sub>2</sub> and 2 h of reaction.

behaviour: yields to HDO and MET products of 52 and 15%, respectively, and phenol as the main product with a yield of 39%.

- Catalysts proved that HDO products formation was the main reaction pathway in any case. Catalysts with  $\beta$ -Mo<sub>2</sub>C crystals favoured the formation of complete deoxygenated products (cyclohexane and benzene). Meanwhile CNF presented a low catalytic activity

reaching a guaiacol conversion of 10% and the formation of toluene as the main product with a yield of 5%, the best catalyst, carburized at 750 °C using a heating rate of 1 °C/min, achieved a guaiacol conversion and a HDO ratio of 67% and 33%, respectively.

#### Acknowledgements

This work was funded by FEDER and the Spanish Economy and Competitiveness Ministry (MINECO) (ENE2014-52189-C02-01-R and ENE2017-83854-R). EO thanks for the award of her PhD under the frame of the aforementioned project. JLP thanks MINECO for his Ramon y Cajal research contract (RYC-2013-12494). The microscopy works have been conducted in the “Laboratorio de Microscopías Avanzadas” at “Instituto de Nanociencia de Aragón - Universidad de Zaragoza”. Authors acknowledge the LMA-INA for offering access to their instruments and expertise. RM is extremely grateful to ICB for partially financing his short term mission at the institution.

#### Appendix A. Supplementary data

Supplementary material related to this article can be found, in the online version, at doi:<https://doi.org/10.1016/j.apcatb.2018.08.043>.

#### References

- [1] Z. He, X. Wang, Hydrodeoxygenation of model compounds and catalytic systems for pyrolysis bio-oils upgrading, *Catal. Sustain. Energy* (2012) 28.

- [2] Q. Lu, W.-Z. Li, X.-F. Zhu, Overview of fuel properties of biomass fast pyrolysis oils, *Energy Convers. Manag.* 50 (2009) 1376–1383.
- [3] M. Saidi, F. Samimi, D. Karimipourfard, T. Nimmanwudipong, B.C. Gates, M.R. Rahimpour, Upgrading of lignin-derived bio-oils by catalytic hydrodeoxygenation, *Energy Environ. Sci.* 7 (2014) 103–129.
- [4] K.L. Deutsch, B.H. Shanks, Hydrodeoxygenation of lignin model compounds over a copper chromite catalyst, *Appl. Catal. A Gen.* 447–448 (2012) 144–150.
- [5] T.V. Choudhary, C.B. Phillips, Renewable fuels via catalytic hydrodeoxygenation, *Appl. Catal. A Gen.* 397 (2011) 1–12.
- [6] E. Butler, G. Devlin, D. Meier, K. McDonnell, A review of recent laboratory research and commercial developments in fast pyrolysis and upgrading, *Renew. Sustain. Energy Rev.* 15 (2011) 4171–4186.
- [7] P.M. Mortensen, J.D. Grunwaldt, P.A. Jensen, K.G. Knudsen, A.D. Jensen, A review of catalytic upgrading of bio-oil to engine fuels, *Appl. Catal. A Gen.* 407 (2011) 1–19.
- [8] A. Gutierrez, R.K. Kaila, M.L. Honkela, R. Slioor, A.O.I. Krause, Hydrodeoxygenation of guaiacol on noble metal catalysts, *Catal. Today* 147 (2009) 239–246.
- [9] A.B. Dongli, I.T. Ghampon, R. Garcia, J.L.G. Fierro, N. Escalona, Hydrodeoxygenation of guaiacol over Ni/carbon catalysts: effect of the support and Ni loading, *RSC Adv.* 6 (2016) 2611–2623.
- [10] P.M. Mortensen, H.W.P. de Carvalho, J.-D. Grunwaldt, P.A. Jensen, A.D. Jensen, Activity and stability of Mo<sub>2</sub>C/ZrO<sub>2</sub> as catalyst for hydrodeoxygenation of mixtures of phenol and 1-octanol, *J. Catal.* 328 (2015) 208–215.
- [11] E. Furimsky, Metal carbides and nitrides as potential catalysts for hydroprocessing, *Appl. Catal. A Gen.* 240 (2003) 1–28.
- [12] M.M. Sullivan, C.-J. Chen, A. Bhan, Catalytic deoxygenation on transition metal carbide catalysts, *Catal. Sci. Technol.* 6 (2016) 602–616.
- [13] V. Heine,  $\delta$ -interaction in transition metals, *Phys. Rev.* 153 (1967) 673–682.
- [14] J.E. Houston, G.E. Laramore, R.L. Park, Surface electronic properties of Tungsten, Tungsten Carbide, and platinum, *Science* 185 (1974) 258–260.
- [15] J.-S. Choi, G. Bugli, G. Djéga-Mariadassou, Influence of the degree of carburization on the density of sites and hydrogenating activity of molybdenum carbides, *J. Catal.* 193 (2000) 238–247.
- [16] J.R.d.S. Politi, F. Vines, J.A. Rodriguez, F. Illas, Atomic and electronic structure of molybdenum carbide phases: bulk and low Miller-index surfaces, *J. Chem. Soc. Faraday Trans. 15* (2013) 12617–12625.
- [17] S. Posada-Pérez, F. Viñes, R. Valero, J.A. Rodriguez, F. Illas, Adsorption and dissociation of molecular hydrogen on orthorhombic  $\beta$ -Mo<sub>2</sub>C and cubic  $\delta$ -MoC (001) surfaces, *Surf. Sci.* 656 (2017) 24–32.
- [18] X. Li, D. Ma, L. Chen, X. Bao, Fabrication of molybdenum carbide catalysts over multi-walled carbon nanotubes by carbothermal hydrogen reduction, *Catal. Lett.* 116 (2007) 63–69.
- [19] D. Mordenti, D. Brodzki, G. Djéga-Mariadassou, New synthesis of Mo<sub>2</sub>C 14 nm in average size supported on a high specific surface area carbon material, *J. Solid State Chem.* 141 (1998) 114–120.
- [20] S. Chaudhury, S.K. Mukerjee, V.N. Vaidya, V. Venugopal, Kinetics and mechanism of carbothermic reduction of MoO<sub>3</sub> to Mo<sub>2</sub>C, *J. Alloys* 261 (1997) 105–113.
- [21] B. Frank, K. Friedel, F. Girgsdies, X. Huang, R. Schlögl, A. Trunschke, CNT-supported Mo<sub>2</sub>C catalysts: effect of loading and carburization parameters, *ChemCatChem* 5 (2013) 2296–2305.
- [22] S. Liu, H. Wang, K.J. Smith, C.S. Kim, Hydrodeoxygenation of 2-Methoxyphenol over Ru, Pd, and Mo<sub>2</sub>C catalysts supported on carbon, *Energy Fuels* 31 (2017) 6378–6388.
- [23] H. Wang, S. Liu, K.J. Smith, Synthesis and hydrodeoxygenation activity of carbon supported molybdenum carbide and oxycarbide catalysts, *Energy Fuels* 30 (2016) 6039–6049.
- [24] H. Wang, S. Liu, B. Liu, V. Montes, J.M. Hill, K.J. Smith, Carbon and Mo transformations during the synthesis of mesoporous Mo<sub>2</sub>C/carbon catalysts by carbothermal hydrogen reduction, *J. Solid State Chem.* 258 (2018) 818–824.
- [25] E. Santillan-Jimenez, M. Perdu, R. Pace, T. Morgan, M. Crocker, Activated carbon, carbon nanofiber and carbon nanotube supported molybdenum carbide catalysts for the hydrodeoxygenation of guaiacol, *Catalysts* 5 (2015) 424.
- [26] S. Ansaloni, N. Russo, R. Pirone, Hydrodeoxygenation of guaiacol over molybdenum-based catalysts: the effect of support and the nature of the active site, *Can. J. Chem. Eng.* 95 (2017) 1730–1744.
- [27] H. Cai, X. An, J. Cui, J. Li, S. Wen, K. Li, M. Shen, L. Zheng, G. Zhang, X. Shi, Facile hydrothermal synthesis and surface functionalization of polyethyleneimine-coated iron oxide nanoparticles for biomedical applications, *ACS Appl. Mater. Interfaces* 5 (2013) 1722–1731.
- [28] J. Chang, T. Danuthai, S. Dewiyaniti, C. Wang, A. Borgna, Hydrodeoxygenation of guaiacol over carbon-supported metal catalysts, *ChemCatChem* 5 (2013) 3041–3049.
- [29] R. Moreira, E. Ochoa, J. Pinilla, A. Portugal, I. Suelves, Liquid-phase hydrodeoxygenation of guaiacol over Mo<sub>2</sub>C supported on commercial CNF. Effects of operating conditions on conversion and product selectivity, *Catalysts* 8 (2018) 127.
- [30] Y. Qin, P. Chen, J. Duan, J. Han, H. Lou, X. Zheng, H. Hong, Carbon nanofibers supported molybdenum carbide catalysts for hydrodeoxygenation of vegetable oils, *RSC Adv.* 3 (2013) 17485–17491.
- [31] L. He, Y. Qin, H. Lou, P. Chen, Highly dispersed molybdenum carbide nanoparticles supported on activated carbon as an efficient catalyst for the hydrodeoxygenation of vanillin, *RSC Adv.* 5 (2015) 43141–43147.
- [32] W.F. Chen, C.H. Wang, K. Sasaki, N. Marinkovic, W. Xu, J.T. Muckerman, Y. Zhu, R.R. Adzic, Highly active and durable nanostructured molybdenum carbide electrocatalysts for hydrogen production, *Energy Environ. Sci.* 6 (2013) 943–951.
- [33] H. Wang, S. Liu, R. Govindarajan, K.J. Smith, Preparation of Ni-Mo<sub>2</sub>C/carbon catalysts and their stability in the HDS of dibenzothiophene, *Appl. Catal. A Gen.* 539 (2017) 114–127.
- [34] C. Sayag, M. Benkhaled, S. Suppan, J. Trawczynski, G. Djéga-Mariadassou, Comparative kinetic study of the hydrodenitrogenation of indole over activated carbon black composites (CBC) supported molybdenum carbides, *Appl. Catal. A Gen.* 275 (2004) 15–24.
- [35] R. Ma, K. Cui, L. Yang, X. Ma, Y. Li, Selective catalytic conversion of guaiacol to phenols over a molybdenum carbide catalyst, *Chem. Commun.* 51 (2015) 10299–10301.
- [36] R. Ma, W. Hao, X. Ma, Y. Tian, Y. Li, Catalytic ethanolysis of kraft lignin into high-value small-molecular chemicals over a nanostructured  $\alpha$ -molybdenum carbide catalyst, *Angew. Chemie* 126 (2014) 7438–7443.
- [37] H. Wang, A. Wang, X. Wang, T. Zhang, One-pot synthesized MoC imbedded in ordered mesoporous carbon as a catalyst for N<sub>2</sub>H<sub>4</sub> decomposition, *Chemical Communications*, DOI 10.1039/B801057A(2008) 2565–2567.
- [38] R. Barthos, A. Széchenyi, F. Solymosi, Efficient H<sub>2</sub> production from ethanol over Mo<sub>2</sub>C/C nanotube catalyst, *Catal. Lett.* 120 (2008) 161–165.
- [39] B. Frank, Z.-L. Xie, K. Friedel Ortega, M. Scherzer, R. Schlögl, A. Trunschke, Modification of the carbide microstructure by N- and S-functionalization of the support in Mo<sub>2</sub>C/CNT catalysts, *Catal. Sci. Technol.* 6 (2016) 3468–3475.
- [40] S. Tuomi, R. Guil-Lopez, T. Kallio, Molybdenum carbide nanoparticles as a catalyst for the hydrogen evolution reaction and the effect of pH, *J. Catal.* 334 (2016) 102–109.
- [41] C. Liang, P. Ying, C. Li, Nanostructured  $\beta$ -Mo<sub>2</sub>C prepared by carbothermal hydrogen reduction on ultrahigh surface area carbon material, *Chem. Mater.* 14 (2002) 3148–3151.
- [42] C. Liang, W. Ma, Z. Feng, C. Li, Activated carbon supported bimetallic CoMo carbides synthesized by carbothermal hydrogen reduction, *Carbon* 41 (2003) 1833–1839.
- [43] J. Pielaszek, B. Mierzwa, G. Medjahdi, J.F. Maréché, S. Puricelli, A. Celzard, G. Furdin, Molybdenum carbide catalyst formation from precursors deposited on active carbons: XRD studies, *Appl. Catal. A Gen.* 296 (2005) 232–237.
- [44] R. Guil-López, E. Nieto, J.A. Botas, J.L.G. Fierro, On the genesis of molybdenum carbide phases during reduction-carburization reactions, *J. Solid State Chem.* 190 (2012) 285–295.
- [45] J. Liang, R. Ding, Y. Wu, Y. Chen, K. Wu, Y. Meng, M. Yang, Y. Wang, Effective conversion of heteroatomic model compounds in microalgae-based bio-oils to hydrocarbons over  $\beta$ -Mo<sub>2</sub>C/CNTs catalyst, *J. Mol. Catal. A Chem.* 411 (2016) 95–102.
- [46] J. Han, J. Duan, P. Chen, H. Lou, X. Zheng, H. Hong, Nanostructured molybdenum carbides supported on carbon nanotubes as efficient catalysts for one-step hydrodeoxygenation and isomerization of vegetable oils, *Green Chem.* 13 (2011) 2561–2568.
- [47] A.L. Jongeri, R.W. Gosselink, J. Dijkstra, J.H. Bitter, P.C.A. Bruijninx, B.M. Weckhuysen, Carbon nanofiber supported transition-metal carbide catalysts for the hydrodeoxygenation of guaiacol, *ChemCatChem* 5 (2013) 2964–2972.
- [48] S.A.W. Hollak, R.W. Gosselink, D.S. van Es, J.H. Bitter, Comparison of tungsten and molybdenum carbide catalysts for the hydrodeoxygenation of oleic acid, *ACS Catal.* 3 (2013) 2837–2844.
- [49] Y.-Y. Wang, L.-L. Ling, H. Jiang, Selective hydrogenation of lignin to produce chemical commodities by using a biochar supported Ni-Mo<sub>2</sub>C catalyst obtained from biomass, *Green Chem.* 18 (2016) 4032–4041.
- [50] D.R. Stellwagen, J.H. Bitter, Structure-performance relations of molybdenum- and tungsten carbide catalysts for deoxygenation, *Green Chem.* 17 (2015) 582–593.
- [51] J.L. Pinilla, S. de Llobet, R. Moliner, I. Suelves, Ni-Co bimetallic catalysts for the simultaneous production of carbon nanofibers and syngas through biogas decomposition, *Appl. Catal. B* 200 (2017) 255–264.
- [52] H.V. Nguyen, S.T. Luu, E.G. Rakov, Solubility of functionalized carbon nanofibers in different aqueous media, fullerenes, Nanotubes Carbon Nanostruct. 20 (2012) 429–433.
- [53] N.T. Hung, N.M. Tuong, E.G. Rakov, Acid functionalization of carbon nanofibers, *Inorg. Mater.* 46 (2010) 1077–1083.
- [54] L. Óvári, J. Kiss, A.P. Farkas, F. Solymosi, Surface and subsurface oxidation of Mo<sub>2</sub>C/Mo(100): low-energy ion-scattering, auger electron, angle-resolved X-Ray photoelectron, and mass spectroscopy studies, *J. Phys. Chem. B* 109 (2005) 4638–4645.
- [55] J. Wienold, Rolf E. Jentoft, T. Ressler, Structural investigation of the thermal decomposition of ammonium heptamolybdate by in situ XAFS and XRD, *Eur. J. Inorg. Chem.* 2003 (2003) 1058–1071.
- [56] M. Pang, C. Liu, W. Xia, M. Muhler, C. Liang, Activated carbon supported molybdenum carbides as cheap and highly efficient catalyst in the selective hydrogenation of naphthalene to tetralin, *Green Chem.* 14 (2012) 1272–1276.
- [57] J.S. Lee, S.T. Oyama, M. Boudart, Molybdenum carbide catalysts, *J. Catal.* 106 (1987) 125–133.
- [58] P. Trucano, R. Chen, Structure of graphite by neutron diffraction, *Nature* 258 (1975) 136.
- [59] K. Oshikawa, M. Nagai, S. Omi, Characterization of molybdenum carbides for methane reforming by TPR, XRD, and XPS, *J. Phys. Chem. B* 105 (2001) 9124–9131.
- [60] Y. Qin, L. He, J. Duan, P. Chen, H. Lou, X. Zheng, H. Hong, Carbon-supported molybdenum-based catalysts for the hydrodeoxygenation of maize oil, *ChemCatChem* 6 (2014) 2698–2705.
- [61] J. Baltrusaitis, B. Mendoza-Sanchez, V. Fernandez, R. Veenstra, N. Dukstiene, A. Roberts, N. Fairley, Generalized molybdenum oxide surface chemical state XPS determination via informed amorphous sample model, *Appl. Surf. Sci.* 326 (2015) 151–161.



- [62] Z. Si, X. Zhang, C. Wang, L. Ma, R. Dong, An overview on catalytic hydrodeoxygenation of pyrolysis oil and its model compounds, *Catalysts* 7 (2017) 169.
- [63] H. Shafaghat, P.S. Rezaei, W.M. Ashri Wan Daud, Effective parameters on selective catalytic hydrodeoxygenation of phenolic compounds of pyrolysis bio-oil to high-value hydrocarbons, *RSC Adv.* 5 (2015) 103999–104042.
- [64] Phenol, *Ullmann's Encyclopedia of Industrial Chemistry*.
- [65] C. Huang, N. Ghavtadze, B. Chattopadhyay, V. Gevorgyan, Synthesis of catechols from phenols via Pd-Catalyzed silanol-directed C–H oxygenation, *J. Am. Chem. Soc.* 133 (2011) 17630–17633.
- [66] Catechol, *Encyclopedia of Reagents for Organic Synthesis*.